Investigating the Impact of Wire Harness Inductance on Hall Thruster Discharge Oscillations

IEPC-2025-513

Presented at the 39th International Electric Propulsion Conference
Imperial College London, London, United Kingdom
September 14-19, 2025

Ajay Krishnan[1], Dan Lev[2], Mitchell Walker[3] and Maryam Saeedifard[4]
Georgia Institute of Technology, Atlanta, Georgia, 30332, USA

Daniel Troyetsky[5], Ken Hara[6]
Stanford University, Stanford, California, 94305, USA

The wire harness is a critical component of the Hall thruster discharge circuit. Its length, and therefore its inductance, can vary between ground tests and spaceflight, leading to differences in discharge oscillations. While the most intuitive strategy would be to minimize harness length by positioning the filter close to the thruster, this is not always feasible. In this work, we investigate the influence of harness inductance on oscillations in discharge voltage, discharge current, cathode-to-ground and thruster-to-ground potentials, power supply current, and plasma parameters using a variable inductor at higher inductances. We find that the discharge voltage increases linearly with harness inductance at 300 V, but exhibits nonlinear behavior and is more oscillatory at 400 V, based on mean normalized analysis. At 300 V, the RMS discharge current peaks at 0.33 A at 39.6 μH, whereas at 400 V, the RMS discharge current reaches a minimum of 0.7 A at 44.6 μH. To further interpret these results, we apply an extended Kalman filter coupled to a zero-dimensional plasma model, yielding time-resolved estimates of ion and neutral number densities, electron temperature, electron axial bulk velocity, and electron cross-field mobility as a function of harness inductance. The analysis shows that heavy species dynamics track the main discharge current oscillation (breathing mode), while electron dynamics contain significant high-frequency components. Furthermore, the normalized RMS oscillation of cross-field electron mobility increases with harness inductance, matching discharge voltage behavior at 300 V and both voltage and current at 400 V. These findings inform thruster and power system integration strategies by highlighting the role of series inductance in shaping discharge oscillations and pointing toward design approaches such as reactive compensation and impedance matching.

I. Nomenclature

m_i = ion mass
n_e = electron density
T_e = electron temperature

[1]Graduate Research Assistant, School of Electrical and Computer Engineering, ajaykrishnan@gatech.edu
[2]Research Engineer, School of Aerospace Engineering, dan.lev@gatech.edu
[3]Chair, School of Aerospace Engineering, mitchell.walker@coe.gatech.edu
[4]Professor, School of Electrical and Computer Engineering, maryam@ece.gatech.edu
[5]PhD Candidate, Department of Aeronautics and Astronautics, dtroyets@stanford.edu
[6]Assistant Professor, Department of Aeronautics and Astronautics, kenhara@stanford.edu

V	=	Voltage	I	=	Current
ID	=	Discharge Current	Z	=	Impedance
VD	=	Discharge Voltage	IPS	=	Power Supply Current
VCG	=	Cathode Body to Ground Voltage	VTBG	=	Thruster Body to Ground Voltage
R	=	Resistance	L	=	Inductance
C	=	Capacitance	VP	=	Power Supply Voltage
CP	=	Power Supply Capacitance	VP	=	Power Supply Voltage
RHP	=	Power Supply Harness Resistance	LHP	=	Power Supply Harness Inductance
CHP	=	Power Supply Harness Capacitance	RF	=	Filter Resistance
CF	=	Filter Capacitance	RHT	=	Thruster Harness Resistance
LF	=	Filter Inductance		=	
LHT	=	Thruster Harness Inductance	CHT	=	Thruster Harness Capacitance
HPEPL	=	High Power Electric Propulsion Laboratory	ODE	=	Ordinary Differential Equation
PPU	=	Power Processing Unit	HET	=	Hall Effect Thruster
VTF	=	Vacuum Test Facility	MFC	=	Mass Flow Controller
BM	=	Breathing Mode	FFT	=	Fast Fourier Transform
PID	=	Proportional-Integral-Derivative	DC	=	Direct Current
AC	=	Alternating Current	K_D	=	Derivative Gain
RMS	=	Root Mean Square	PP	=	Peak-to-Peak
K_P	=	Proportional Gain	K_I	=	Integral Gain

II. Introduction

A HET is a plasma device that generates thrust via the electrostatic acceleration of ions [1, 2]. First developed in the 1960s, HETs have been increasingly used as a propulsion option for satellites due to their mass savings as compared to chemical propulsion devices [2]. To increase their usage in satellites and deep space missions, it is critical to advance HET technology by increasing thrust, specific impulse, efficiency, and lifetime. The development of HET technology requires operating HETs in ground-based vacuum facilities while replicating the conditions of the space environment. However, it is not possible to fully emulate space conditions on the ground, leading to unintended deviation in thruster behavior as measured in space [3].

Vacuum chambers introduce "facility effects" that change thruster performance and thruster plume and discharge physics on the ground compared to space [3–6]. Facility effects occur because ground facility pumping systems cannot reach the low-pressure levels that exist in space [7]. In addition, the existence of a large conductive chamber walls creates current paths that otherwise do not exist in the space environment [3–6]. Lastly, sputtering, emanating from the chamber walls back onto and into the thruster may interfere with the HET discharge and affect lifetime [3]. Thus, it is critical to understand the influence of various facility-related factors on HET physics and operation and to be able to correctly determine space performance based on ground testing.

Discharge current oscillations are the result of plasma instabilities in a HET discharge [8, 9]. Of the various HET oscillation types, the predominant type is the so-called BM oscillation that is tied to predator-prey interactions between electrons and neutrons in the discharge plasma [10]. They present plasma parameter variations, specifically plasma density, in the discharge chamber of the HET. BM oscillatory dynamics can be expressed through the conservation of mass, momentum, and energy equations and can be used to define the discharge plasma as an electrical load [11]. This dominant mode occurs in the tens of kHz range and can lead to discharge current amplitudes greater than 100% of the mean [10]. It plays a significant role in the dynamics and performance of a HET, as highly oscillatory thrusters have been shown to exhibit reduced lifetimes [2].

Data collected from space missions have revealed performance disparities between space and ground conditions. We aim to understand and eliminate such discrepancies caused by differences created by the electrical harnessing of HETs, known as harness facility effects [12–14]. The electrical harness, a vital component of the discharge circuit as shown in

Figure 1 with a lumped component model, has different lengths and thus inductance between ground-based development testing and operation on the spacecraft. The differences in inductance result in differences in the voltage oscillations of HET [12]. Any harnessing that may exist between the PPU and the discharge filter is referred to as the power supply harness, whereas any harnessing between the discharge filter and the HET is referred to as the thruster harness. Due to the discharge filter, the power supply harness does not significantly contribute to oscillations, thus we can often ignore it. In the thruster harness, CHT is often very small and negligible, leaving RHT and LHT being the most significant sources of oscillations. The origin of the voltage oscillation comes from the time-varying discharge current that flows through the inductor, as shown in Equation 1. The discharge voltage oscillations could compromise the operation of the thruster if their amplitudes exceed a certain threshold. To address this issue, it is generally recommended to minimize the harness length and inductance by relocating the filter close to the thruster. While relocating the filter holds the potential to increase harness inductance and subsequently decrease system complexity and costs, it is important to note that this physical configuration may not always be feasible. Alternative options to mitigate inductance include employing engineering techniques like busbars, although this approach may present challenges, particularly in the context of spacecraft applications [12].

$$V = L\frac{dI}{dt} \tag{1}$$

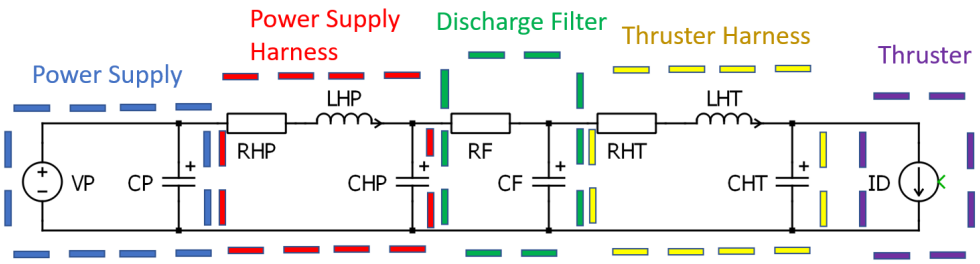

Fig. 1 Discharge Circuit Diagram

Past work on harness analysis was performed Pinero et al. at the NASA Glenn Research Center and by Brieda et al. [12, 13]. Pinero focused on an experimental approach while Brieda focused on a simulation approach. Pinero used a breakout box with changeable components to vary the inductance of the harness. Pinero and Brieda determined that voltage oscillations scale linearly with inductance at lower inductances, but as inductance increases, Brieda shows that voltage oscillations begin to decrease. This might be due to nonlinear effects between the harness inductance and the discharge plasma, where current oscillations are reduced, leading to reduced voltage oscillations. However, Brieda's computational results have not been verified experimentally. It is thus important to experimentally determine the effects of higher inductance levels. Higher inductances could, in fact, reduce oscillations due to nonlinear impedance interactions with the HET load.

This paper presents an experimental and computational effort to characterize the effect of harness inductance on discharge voltage, discharge current, cathode body to ground, thruster body to ground, power supply current, and plasma parameter oscillations. We outline how additional harness inductance can act as a form of passive control for the HET system by changing impedance and thus potentially reactive power and power factor, illustrated in Figure 2, rather than simply placing the discharge filter close to the thruster. Inductance control is a more specific case of RLC control, outlined by Barral, which acts as a PID controller, as shown in Equation 2 [15–18]. RF behaves as K_P, LF behaves as K_I, and CF behaves as K_D. However, the harness inductance does not play the same role as the filter inductance in an RLC filter, as it appears directly in series with the HET load, leading to different impedance effects.

$$I_D = \frac{V_P - V_D}{R_F} + \frac{1}{L_F}\int_0^t (V_P - V_D)\,dt - C_F\frac{dV_D}{dt} \tag{2}$$

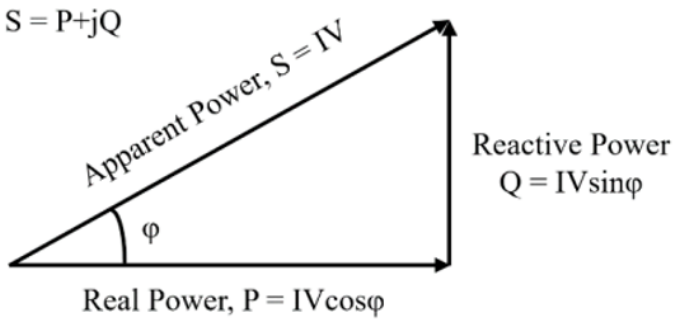

Fig. 2 Power Triangle

III. Methods

Section A discusses the vacuum test facility that was used to conduct experimentation on the HET. Section B discusses the specific thruster used and its setup and operation. Section C explains the data collection process, and lastly, Section D describes uncertainty quantification for the experiment.

A. Vacuum Facility

The harness experiment was performed in VTF-2 at Georgia Tech's High-Power Electric Propulsion Laboratory. An image of this facility is shown in Figure 3b. VTF-2 is a stainless-steel chamber measuring 4.9 m in diameter and 9.2 m in length. Rough vacuum in VTF-2 is established using one 495 CFM rotary-vane pump and one 3800 CFM blower. High vacuum is attained using ten liquid nitrogen-cooled CVI TMI re-entrant cryopumps at a pumping speed of 350,000 l/s on xenon. The cryopump shrouds are fed using the Stirling Cryogenics SPC-8 RL special closed-loop nitrogen liquefaction system [19].

B. H6 HET Setup and Operation

We used the H6 HET in this study, shown in Figure 3a, a 6-kW class HET developed in partnership between the NASA Jet Propulsion Laboratory, the Air Force Research Laboratory, and the University of Michigan [1]. The H6 uses a centrally mounted LaB_6 cathode. The thruster body and cathode were isolated from facility ground and were electrically floating.

(a) H6 HET. **(b) VTF-2.**

Fig. 3 H6 HET and VTF-2

The H6 discharge plasma was controlled using a Magna-Power TS800-24 power supply. Other thruster components were powered using TDK-Lambda GEN80-42 power supplies. A TDK-Lambda GEN600-2.6 and GEN60-25 were used

to power the cathode keeper and heater, respectively. For protection, the discharge supply was connected to a low-pass RC discharge filter consisting of a series 0.533-Ohm resistor and a shunt 100-µF capacitor to attenuate discharge current oscillations greater than 3 kHz in frequency.

High-purity (99.999%) krypton was fed into the anode and cathode propellant lines using stainless-steel lines metered with MKS GE50A MFCs. The MFCs were calibrated by measuring the flow upstream of the thruster with a MesaLabs DryCal 800-10 volumetric flow meter. The uncertainty for flow in the anode and cathode lines is 2% and 5%, respectively.

The anode and cathode flow rate and the magnetic field were kept constant during testing. Table 3 shows the H6 HET operating points that were used during experimentation, at discharge voltages of 300 V and 400 V. Upon ignition, the H6 HET was run for three hours until its oscillations became steady after outgassing. The base facility pressure was 10 nTorr, while the facility pressure during operation was 2 μTorr. A motorized software-controlled variable inductor was utilized to adjust the inductance of the harness at 19 inductance values.

Inductance Test Matrix (µH): 16.6, 19.6, 24.6, 29.6, 34.6, 39.6, 44.6, 49.6, 54.6, 59.6, 64.6, 69.6, 74.6, 79.6, 84.6, 89.6, 94.6, 99.6, 104.6

Table 3 H6 HET Operating Conditions

Discharge Voltage (V)	Discharge Current (A)	Anode Flow Rate (sccm)	Cathode Flow Rate (sccm)	Inner Coil Current (A)	Outer Coil Current (A)	Breathing Mode Frequency (kHz)
300	4.3	65	6.5	2.15	1.96	10
400	4.3	65	6.5	2.15	1.96	13

C. Data Collection

The discharge voltage, AC discharge current, cathode body to ground, thruster body to ground, and power supply current oscillations of the H6 HET were recorded using Teledyne LeCroy CP150 and T3CP150 current probes, a Pearson 110A current monitor placed inside VTF2, and HVD3106A and T3HVD1500-70 voltage probes connected to HDO6054 and HDO6104 Teledyne LeCroy oscilloscopes synchronized using an external clock and trigger. The uncertainty and bandwidth of the current probe are ±1% and 10 MHz; for the oscilloscope, they are ±0.5% full scale and 1 GHz. The oscilloscope has 12 bits of resolution with a selected 25 MS/s sampling rate and is used over an interval of 10 ms for a total of 250,000 samples. MATLAB instrument control toolbox with USB and Ethernet for remote desktop were used for semi-automated data collection. Thruster data was taken after it was observed that the PP discharge current values had stopped changing within ±1% variation, taking approximately two hours.

D. Uncertainty Quantification

Systematic and random errors were quantified as part of this study's error analysis. Systematic errors are introduced by voltage and current probe measurement uncertainty, along with the oscilloscope's uncertainty in the acquired data. These uncertainties were defined in the data collection subsection.

IV. Results and Discussion

We first present results on the electrical effects of varying harness inductance on the HET discharge plasma. For the 300 V and 400 V conditions, we show RMS plots of discharge voltage, discharge current, cathode body-to-ground voltage, thruster body-to-ground voltage, mean plots of cathode body-to-ground voltage and thruster body-to-ground voltage, and a PP plot of power supply current, all as a function of harness inductance. To better aid analysis, we plot mean normalized quantities for better comparison between the two operating points.

Figure 4a shows that the BM frequency at 300 V attains a minimum of 6.5 kHz at 34.6 μH and a maximum of 8.5 kHz at 89.6 μH at 300 V. At 400 V, Figure 4b shows that a minimum of 9 kHz is attained at 34.6 μH and 39.6 μH, with a maximum of 11.25 kHz at 16.6 μH. At both voltages, the BM frequency roughly decreases, then increases.

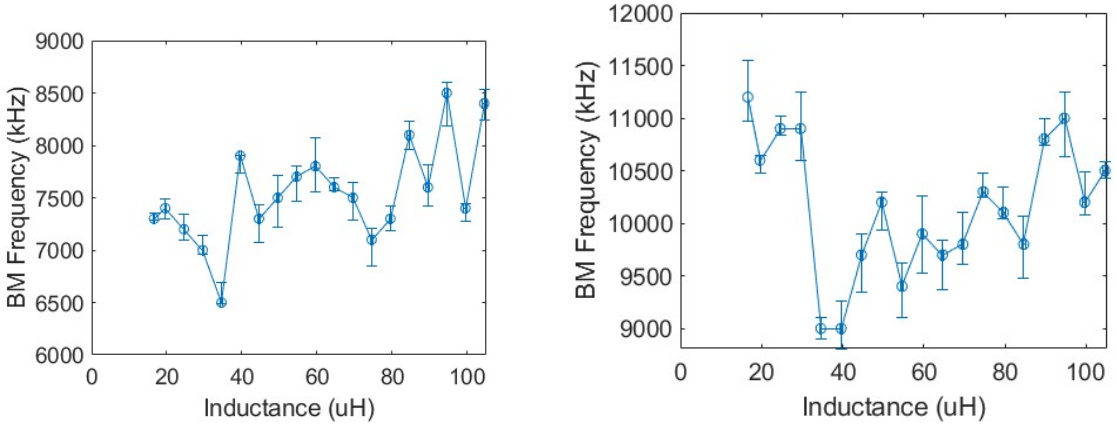

(a) 300 V Case **(b) 400 V Case**

Fig. 4 BM Frequency as a Function of Inductance

Figure 5a and Figure 5b show that the RMS of the discharge voltage oscillations increase with increasing inductance, as expected from the inductor equation relating voltage to inductance and the time derivative of current. The 300 V RMS ranges from 3 to 8 V across the inductance range, whereas the 400 V RMS ranges from 6 to 19 V, however the 400 V curve appears to be nonlinear while the 300 V curve appears to be linear. It is important to note that the RMS normalized by the oscillation mean does not match between operating conditions, where at 300 V percentages range from 2% to 3%, whereas for 400 V percentages range from 2% to 5%. The 400 V operating condition is more oscillatory with a higher BM frequency, which results in a larger percentage of the mean oscillation.

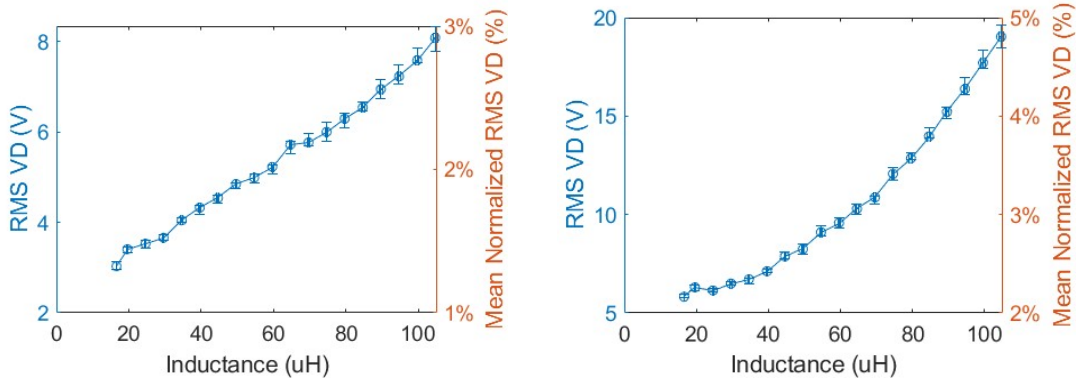

(a) 300 V Case **(b) 400 V Case**

Fig. 5 RMS Discharge Voltage as a Function of Inductance

Figure 6a shows that the RMS discharge current at 300 V increases to a maximum of 0.325 A at around 39.6 μH of inductance, then continues to decrease as inductance increases. On the other hand, the 400 V condition shown in Figure 6b reaches a minimum RMS of 0.7 A, respectively, at 44.6 μH, rather than a maximum, then begins increasing with increasing inductance. The 300 V RMS ranges from 0.21 to 0.33 A across the inductance range, whereas the 400 V RMS ranges from 0.7 to 2 A. Again, the RMS normalized by the oscillation mean does not match between operating conditions, where at 300 V percentages range from 5% to 5.8% for RMS, whereas for 400 V the RMS ranges from 16% to 41%. It is clear that the 400 V operating condition is more oscillatory, which results in a larger percentage of the mean oscillation.

The current oscillations are maximized for the 300 V case and minimized for the 400 V case at 39.6 μH and 44.6 μH, respectively, due to nonlinear impedance interactions with the HET impedance. Plasma state estimation could further explain what may be occurring in the plasma that could better explain these findings by revealing more about the

corresponding plasma parameter dynamics.

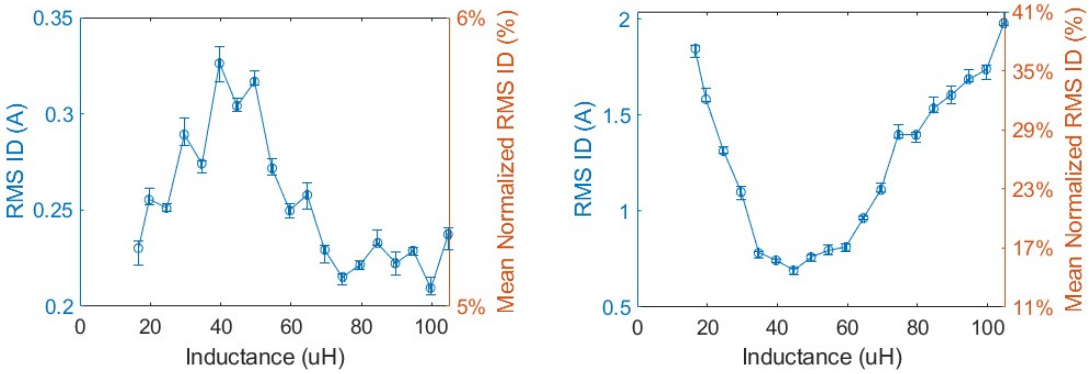

(a) 300 V Case **(b) 400 V Case**

Fig. 6 RMS Discharge Current as a Function of Inductance

Figure 7a shows that the RMS cathode body-to-ground voltage at 300 V attains a minimum of 1.525 V between 64.6 and 99.6 µH. On the other hand, the 400 V condition shown in Figure 7b reaches a minimum RMS of 2.5 V at 44.6 μH, which is tied to improved electron emission. The 300 V RMS ranges from 1.525 to 1.825 V across the inductance range, whereas the 400 V RMS ranges from 2.41 V to 4.1 V. At 300 V, mean normalized RMS percentages range from 9.1% to 9.7%, whereas for 400 V RMS percentages ranges from 15% to 19.5%. It is not quite clear why 89.6 μH minimizes the oscillations at 300 V.

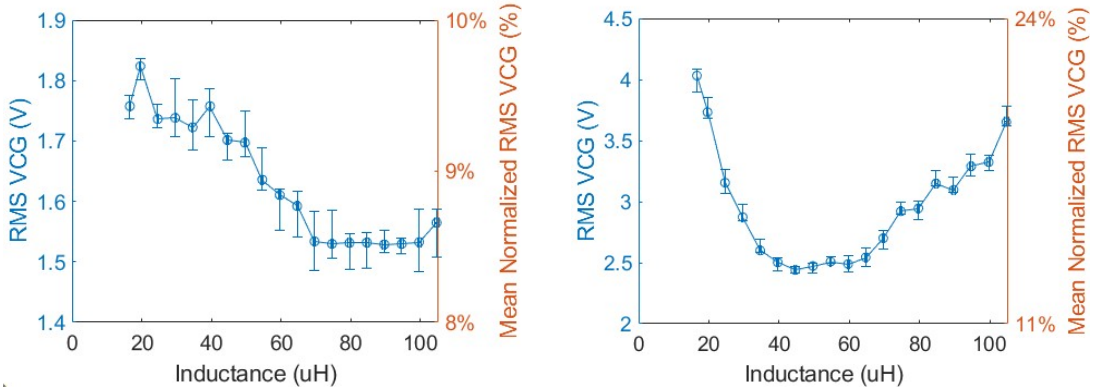

(a) 300 V Case **(b) 400 V Case**

Fig. 7 RMS Cathode Body-to-Ground Voltage as a Function of Inductance

Figure 8a shows that at 300 V, the RMS thruster body-to-ground voltage increases to a peak of 3.3 V at 39.6 μH, then decreases. On the other hand, the 400 V condition shown in Figure 8b reaches a minimum RMS of 8 V at 39.6 μH. The 300 V RMS ranges from 2.07 to 3.3 V across the inductance range, whereas the 400 V RMS ranges from 8 to 15 V. For the RMS at 300 V, the mean normalized percentages range from 54% to 76% for RMS, whereas for 400 V the RMS ranges from 44% to 85%.

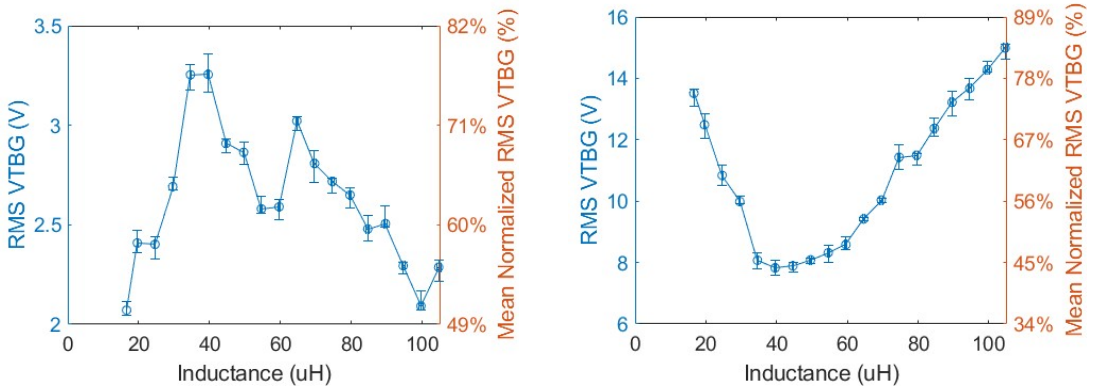

(a) 300 V Case **(b) 400 V Case**

Fig. 8 RMS Thruster Body-to-Ground Voltage as a Function of Inductance

Figure 9a shows that at 300 V the mean cathode body-to-ground voltage reaches a maximum of -17.78 V at 29.6 μH, then decreases to -18.2 V at 64.6 μH, where it then stays relatively constant until 104.6 μH. At 400 V, shown in Figure 9b, the mean cathode body-to-ground voltage reaches a maximum of -17.825 V at around 44.6 μH from a minimum of -18.625 V at 19.6 μH, and then begins to decrease. It is evident that the 400 V operating condition has roughly the same mean cathode body-to-ground voltage of -18 V as the 300 V condition.

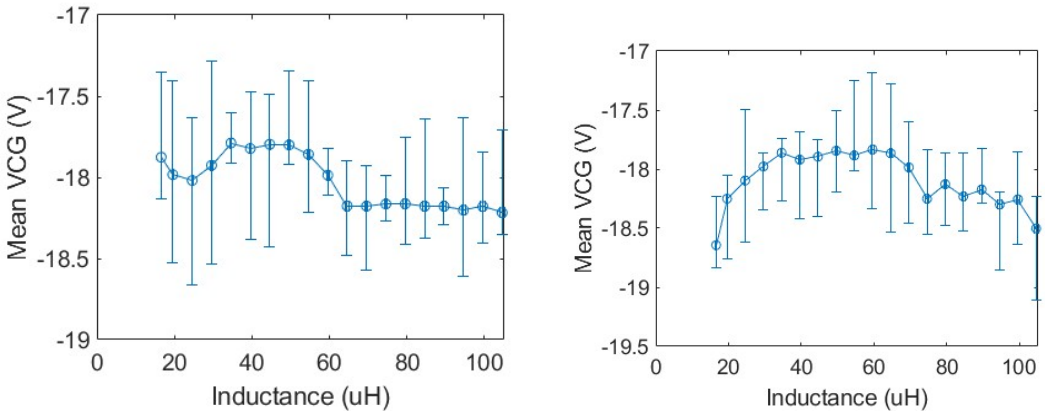

(a) 300 V Case **(b) 400 V Case**

Fig. 9 Mean Cathode Body-to-Ground Voltage as a Function of Inductance

Figure 10a shows that the mean thruster body-to-ground voltage reaches a minimum of -8.5 V at around 34.6 µH and increases to a maximum of -4.1 V at 104.6 μH. At 400 V, shown in Figure 10b, the mean thruster body to ground voltage has a maximum of around -11.75 V at 44.6 μH, then continues to decrease to a minimum of -18 V at 104.6 μH at 400 V. The thruster mean body to ground voltage is lower at 400 V at around -14 V on average as opposed to -6.5 V on average at 300 V. This suggests that the thruster body is at a much lower potential than ground at 400 V, which would indicate there to be more ion current flow from the plasma to the thruster body.

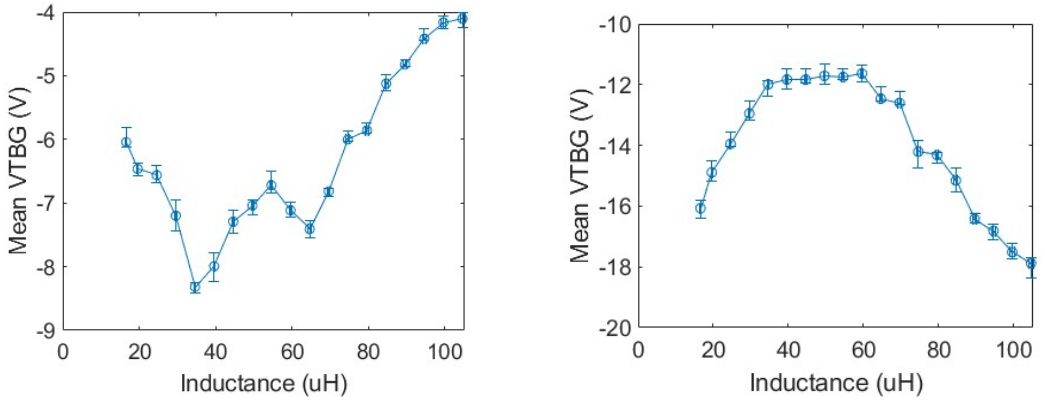

(a) 300 V Case **(b) 400 V Case**

Fig. 10 Mean Thruster Body-to-Ground Voltage as a Function of Inductance

Figure 11a shows that the PP power supply current at 300 V reaches a minimum of 0.33 A at 94.6 μH compared to a maximum of 0.45 A at 39.6 μH. Figure 11b shows that at 400 V the PP power supply current reaches a minimum of 0.65 A at 44.6 μH compared to a maximum of 0.97 A at 104.6 μH. For the PP at 300 V, the mean normalized percentages range from 7.4% to 9% for RMS, whereas for 400 V the RMS ranges from 15% to 19.5%. These results show that the power supply current oscillations do in fact change with harness inductance.

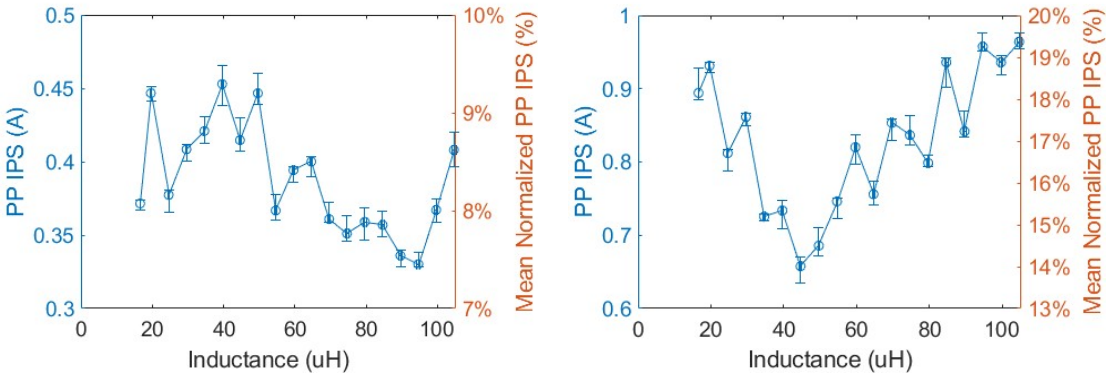

(a) 300 V Case **(b) 400 V Case**

Fig. 11 PP Power Supply Current as a Function of Inductance

These results comprise data that has not been collected before and provide more insight into the operation of a HET at different harness inductances. The mean normalized RMS figures show that the 400 V condition is more oscillatory than the 300 V condition. Maxima and minima exist across the characterized inductance range. There is potential for rich physics insights to be made with the aid of plasma state estimation.

V. Circuit-plasma coupling

We hypothesize that the nonlinear behavior of the discharge current and voltage oscillations as the harness inductance is changed is due to the coupling between the discharge circuit and the HET plasma. To better understand the underlying plasma physics, a zero-dimensional (0D) global plasma model of a HET is used in conjunction with an extended Kalman filter (EKF) to provide estimates of spatially-averaged, time-resolved plasma properties [11, 20, 21].

A. Global plasma model

The 0D global model consists of the ion and neutral continuity equations and the electron energy equation:

$$\frac{\partial N_i}{\partial t} + \frac{N_i U_i}{L_p} + \frac{2N_i U_{i,w}}{R_\Delta} = N_i N_n \zeta_{ion}, \tag{3}$$

$$\frac{\partial N_n}{\partial t} + \frac{(N_n - N_{int})U_n}{L_p} = -N_i N_n \zeta_{ion}, \tag{4}$$

$$\frac{\partial}{\partial t}\left(\frac{3}{2}N_i T_e\right) + \frac{5}{2}\frac{N_i U_e T_e}{L_p} = S_j - S_w - S_c, \tag{5}$$

where the ion bulk velocity is approximated as $U_i = \sqrt{eV_d/M_i}$, e is the elementary charge, V_d is discharge voltage, M_i is ion mass, and $U_{i,w}$ is the ion bulk velocity towards the wall accounting for radial ion losses [22]. Here, $U_{i,w} = \sqrt{eT_e/M_i}$ is the Bohm velocity, T_e is the electron temperature in eV, R_Δ is the channel width, $N_{int} = \dot{m}(M_i A_c U_n)^{-1}$ is the number density of neutral particles injected at the anode, U_n is the neutral bulk velocity which is assumed to be constant, A_c is the thruster cross-sectional area, $\dot{m}$ is the mass flow rate, and ζ_{ion} is the ionization rate, given as

$$\zeta_{ion} = \sqrt{\frac{8eT_e}{\pi m_e}}\left[A_i T_e^2 + B_i \exp\left(-\frac{C_i}{T_e}\right)\right], \tag{6}$$

where for krypton, $A = -1.1592 \times 10^{-24}$, $B = 4.9527 \times 10^{-20}$, $C = 14.0$, and m_e is the mass of an electron. The coefficients A, B, and C for krypton are determined by fitting to rate coefficient data obtained from the Biagi database [23], assuming a Maxwellian electron energy distribution function. The ionization rate coefficient and fitting function are shown in Fig. 12. The proposed fitting function follows the procedure used for xenon in Ref 2. In equation (5), $S_j = -N_i U_e E$ is the energy gain due to Joule heating, U_e is the electron bulk velocity, $E \approx V_d/L_p$ is the electric field strength, $S_w = N_i \epsilon_w \nu_w$ is the energy loss due to interactions with the channel wall, $S_c = \chi N_i N_n \zeta_{ion} \epsilon_{ion}$ is the energy loss due to inelastic ion collisions, χ is the ionization cost accounting for inelastic energy loss, and ϵ_{ion} is the energy loss of electrons due to ionization. The ionization cost is assumed to be a constant value. The wall collision frequency is given as

$$\nu_w = \frac{1}{R_\Delta}\sqrt{\frac{eT_e}{M_i}}\frac{1}{1-\sigma}, \tag{7}$$

where σ is the effective rate of secondary electron emission. For krypton and boron nitride channel walls, at $T_e \leq 24.5\ eV$, $\sigma = T_e/25$, otherwise the sheath is considered to be space charge limited (SCL) and $\sigma = 0.979$ [24]. The energy loss to the wall is described as

$$\epsilon_w = 2T_e + (1-\sigma)\phi_w, \tag{8}$$

where

$$\phi_w = T_e \ln \frac{1-\sigma}{\sqrt{2\pi m_e/M_i}} \tag{9}$$

is the sheath potential [9, 10, 25].

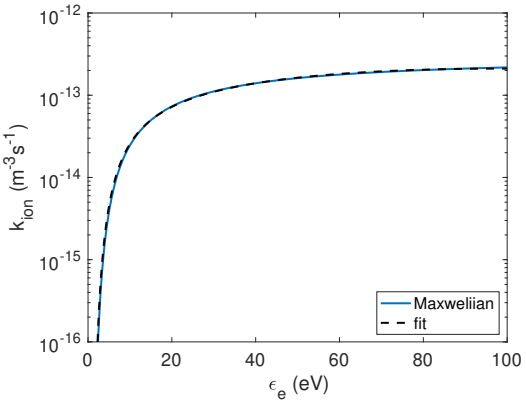

Fig. 12 Ionization rate coefficient and approximate fitting function for krypton.

The discharge current in the channel of the HET, which will be used as the measurement signal for the EKF, can be calculated as

$$I_d = eA_c N_i \left(U_i - U_e\right). \tag{10}$$

After data assimilation, the cross-field electron mobility can be estimated as $\mu_\perp \approx -U_e/E$ assuming that the drift due to the electric field dominates over that of the pressure gradient, which cannot be captured in a 0D model.

B. Extended Kalman filter

For a dynamical system with a state vector $\boldsymbol{x}(t)$, the extended Kalman filter (EKF) consists of an estimated state vector $\hat{\boldsymbol{x}}(t)$, measurement vector $\tilde{\boldsymbol{y}}(t)$, system covariance matrix $P(t)$, measurement noise covariance matrix $R(t)$, process noise covariance matrix $Q(t)$, and noise gain matrix $G(t)$, where each of these quantities can depend on time. The goal of the EKF is to provide an estimate of the underlying states as functions of time which reproduce $\tilde{\boldsymbol{y}}(t)$. At some discrete timestep, k, when the model acquires a measurement, *i.e.*, data, the predicted state denoted with (-) will be corrected to an updated state denoted using (+), as follows:

$$\hat{\boldsymbol{x}}_k^+ = \hat{\boldsymbol{x}}_k^- + K_k\left[\tilde{\boldsymbol{y}}_k - \boldsymbol{h}\left(\hat{\boldsymbol{x}}_k^-\right)\right], \tag{11}$$

$$P_k^+ = [\mathbb{I} - K_k H_k(\hat{\boldsymbol{x}}_k^-)]P_k^-, \tag{12}$$

where $\mathbb{I}$ is the identity matrix, $\boldsymbol{h}$ is the vector of measurement equations, $H_k\left(\hat{\boldsymbol{x}}_k^-\right) = \partial \boldsymbol{h}/\partial \boldsymbol{x}|_{\hat{\boldsymbol{x}}_k^-}$ is the measurement Jacobian matrix, and K_k is the Kalman gain, calculated as

$$K_k = P_k^- H_k^T\left(\hat{\boldsymbol{x}}_k^-\right)\left[H_k\left(\hat{\boldsymbol{x}}_k^-\right) P_k^- H_k^T\left(\hat{\boldsymbol{x}}_k^-\right) + R_k\right]^{-1}. \tag{13}$$

Here, the continuous-discrete EKF is used. Rather than apply equations (11) and (12) at each timestep, a set of equations, i.e., Eqs. (3)-(5), are used to govern the continuous propagation of states between the arrival of measurement data at some discrete time. This set of equations can be interpreted as a physical model of the expected system dynamics and is generally given as

$$\dot{\hat{\boldsymbol{x}}} = \boldsymbol{f}(\hat{\boldsymbol{x}}, t), \tag{14}$$

$$\dot{P} = F(\hat{\boldsymbol{x}}, t)P + PF^T(\hat{\boldsymbol{x}}, t) + GQG^T, \tag{15}$$

where $\boldsymbol{f}$ is the dynamics model function of the state variables and $F(\hat{\boldsymbol{x}}, t) = \partial \boldsymbol{f}/\partial \boldsymbol{x}|_{\hat{\boldsymbol{x}}}$ is the Jacobian matrix of the dynamics model. The combination of Eqs. (11)-(12) and (14)-(15) can be viewed as a predictor-corrector method, where Eqs. (14)-(15) describe the continuous propagation in time of the state quantities through the dynamics (physics-based) model and equation (11)-(12) augment the state values based on the measurement.

For this analysis, the state variables for the EKF are taken to be $\boldsymbol{x} = [N_i\ N_n\ T_e\ U_e]^T$. The electron velocity, U_e, is considered to be an unknown parameter and therefore is only updated when a new measurement arrives (i.e., $dU_e/dt = 0$). A provided discharge current signal is used as the measurement signal, $\tilde{\boldsymbol{y}} = \tilde{I}_d$, and is estimated using equation (10). Here, $\boldsymbol{f}$ is defined by Eqs. (3), (4), and (5) as well as $\partial U_e/\partial t = 0$, and $\boldsymbol{h}(\boldsymbol{x})$ is given by equation (10).

C. State estimation results

The fusion of the experimental data (i.e., discharge current and discharge voltage) with the 0D global plasma model using the EKF allows for the estimation of spatially-averaged, time-resolved plasma properties. The model is run for each combination of harness inductance and operating condition, yielding 38 separate simulations. Examples of the time-resolved state estimates are shown in Figs. 13a and 13b for a harness inductance of 100 μH for the 300 V and 400 V cases, respectively. Each plot shows the normalized waveform of the experimental discharge current trace alongside those of the estimated ion number density, neutral number density, electron temperature, electron bulk velocity, and electron cross-field mobility. Although the details of the oscillations vary with harness inductance and operating condition, several qualitative observations remain constant. The waveforms show predominantly low-frequency (BM) sinusoidal behavior in the discharge current, ion number density, and neutral number density, and high-frequency non-sinusoidal behavior in the electron temperature, electron bulk velocity, and cross-field electron mobility. This implies that the BM oscillation is largely driven by the predator-prey interaction between ions and neutrals, consistent with previous findings [9].

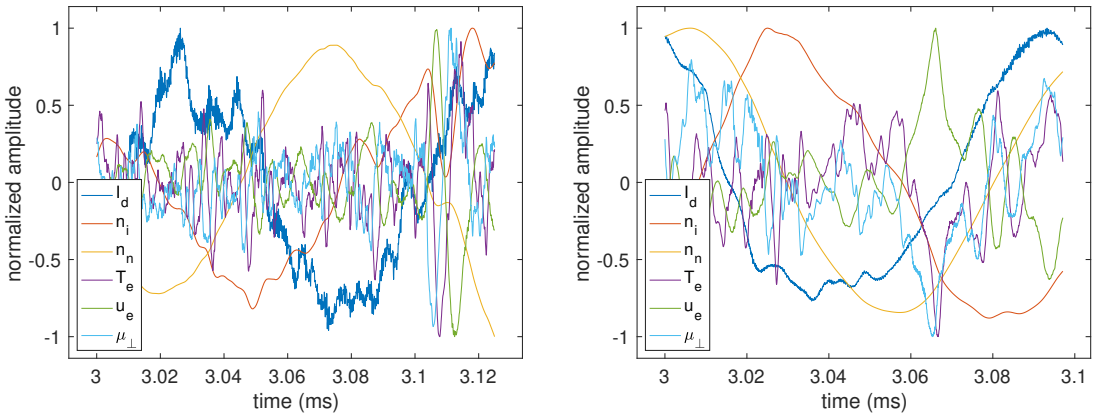

(a) Waveforms with 100 μH harness at 300 V **(b) Waveforms with 100 μH harness at 400 V**

Fig. 13 Plots of the normalized waveforms for the experimental discharge current and estimated ion number density, neutral number density, electron temperature, electron bulk velocity, and electron cross-field mobility as functions of time with 100 μH harness inductance at (left) 300 V and (right) 400 V.

A more convenient way to visualize the dependence of the plasma oscillations on the harness inductance is by comparing the normalized RMS oscillation amplitudes of all quantities, as is shown in Figs. 14a and 14b for the 300 V and 400 V case, respectively. Although not shown here, the time-averaged (i.e., mean) values of all properties remain constant regardless of harness inductance. The discharge currents and discharge voltages shown in these figures correspond to those in Figs. 7 and 8. At both operating conditions, Figs. 14a and 14b show that the ion and neutral number densities normalized RMS amplitudes closely follow the trend of the discharge current, consistent with the waveforms shown in Figs. 13a and 13b. At 300 V, Fig. 14a demonstrates that the electron temperature normalized RMS amplitudes tend to decrease with increased harness inductance but reach a minimum at around 85 μH. The cross-field mobility increases slowly at low inductance and then closely follows the trend of the discharge voltage beginning at around 85 μH. This change in the oscillatory behavior of the electron properties may suggest an increased coupling between the plasma and circuit at large harness inductance.

As shown in Fig. 13b, the behavior at 400 V appears to be more nonlinear, showing approximately the same RMS oscillation amplitude for the discharge current, ion density, and neutral density at 15 μH and 105 μH with a large decrease in between. The discharge voltage RMS oscillation amplitude again increases with harness inductance, but no longer linearly. The electron temperature and electron velocity RMS oscillation amplitudes sharply decrease until 40 μH before plateauing. The electron velocity RMS oscillation amplitude then increases slightly with harness inductance. Perhaps most interesting is the cross-field electron mobility, which qualitatively follows the discharge current in shape but does not experience as large a decrease in RMS oscillation amplitude. At large harness inductance, both the discharge current and discharge voltage increase sharply in amplitude, and so it is difficult to determine which is more closely correlated with the electron mobility. Additional analysis such as convergent cross mapping would be needed to address causality.

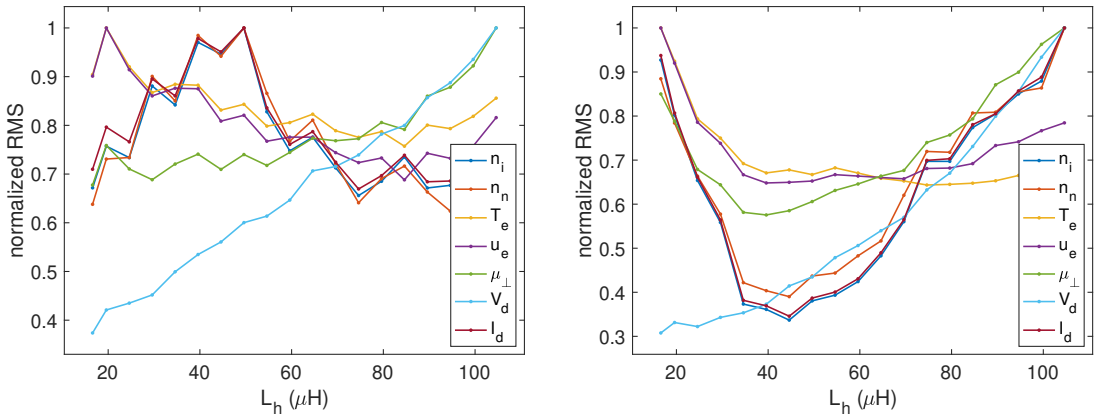

(a) State RMS amplitudes at 300 V **(b) State RMS amplitudes at 400 V**

Fig. 14 Normalized RMS oscillation amplitudes for all estimated plasma properties, along with the discharge current and discharge voltage, at (left) 300 V and (right) 400 V operating conditions.

Figures 15a and 15b show the dimensional cross-field mobility as a function of harness inductance, with the error bars indicating the amplitude of the RMS oscillations. Here, it can clearly be seen that the time-averaged cross-field mobility is constant with harness inductance. This implies that the harness length does not affect the resistance of the plasma, but only its reactance. This interaction further implies nonlinear coupling between the linear circuit upstream of the thruster and the plasma load.

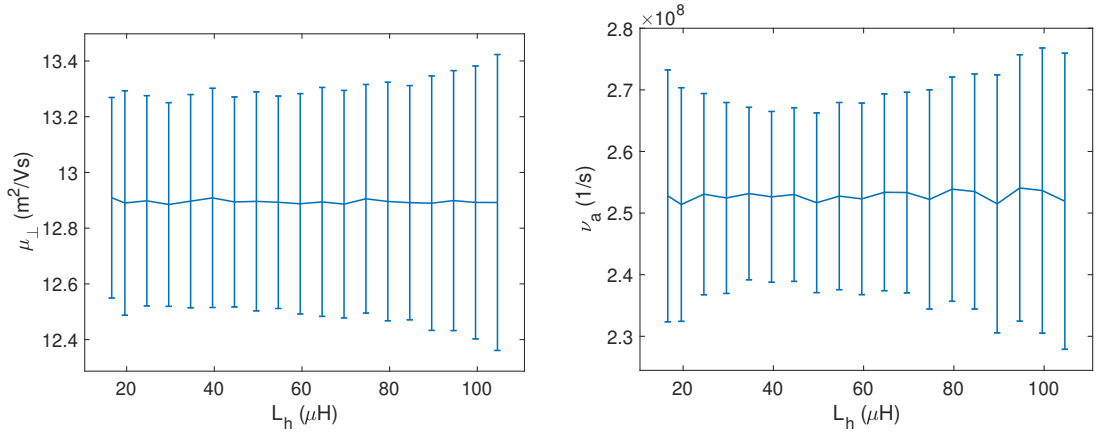

(a) Electron cross-field mobility at 300 V **(b) Electron cross-field mobility at 400 V**

Fig. 15 Mean cross-field electron mobility as a function of harness inductance for the (left) 300 V and (right) 400 V operating conditions. The bars show the RMS oscillation amplitudes.

VI. Conclusion

This work characterizes discharge voltage, discharge current, cathode body-to-ground, thruster body-to-ground, power supply current, and plasma parameter oscillations as a function of harness inductance at two HET operating points. We found that there exists a nonlinear coupling between the harness inductance and oscillatory behavior in a HET through impedance interactions. The RMS of the oscillations exhibit minima and maxima in their characteristic curves as functions of harness inductance. Harness inductance not only affects the electrical dynamics but also affects the plasma dynamics of the HET, changing cathode emission along with thruster body potentials that alter electrical pathways. These findings support the conclusion that while shorter harnesses minimize discharge voltage oscillations, there may exist a different optimal harness length or inductance that can reduce discharge current oscillations. A detailed analysis of the coupling between the discharge circuit and plasma discharge is reserved for future work.

Acknowledgments

The authors would like to thank all of the undergraduate and graduate student researchers at HPEPL that contributed towards experimental setup and vacuum facility operation, particularly Julian Lopez-Uricoechea, Will Brabston, Nafez Ahmmed, Frank George, Hector Sanchez, Irene Moxley, and Daniel Wochnick. Lastly, the authors would like to thank the NASA Joint Advanced Propulsion Institute for its support under the grant number 80NSSC21K1118.

References

[1] Brown, D. L., "Investigation of low discharge voltage Hall thruster operating modes and ionization processes," *31st International Electric Propulsion Conference*, Ann Arbor, MI, USA, 2009. IEPC-2009-074.

[2] Goebel, D., and Katz, I., *Fundamentals of Electric Propulsion: Ion and Hall Thrusters*, Wiley, Hoboken, NJ, 2008.

[3] Byers, D., "A review of facility effects on Hall effect thrusters," *31st International Electric Propulsion Conference*, Ann Arbor, MI, USA, 2009. IEPC-2009-076.

[4] Frieman, J. D., "Role of a conducting vacuum chamber in the Hall Effect Thruster Electrical Circuit," *Journal of Propulsion and Power*, 2014.

[5] Byrne, M. P., Roberts, P. J., and Jorns, B. A., "Coupling of electrical and pressure facility effects in Hall effect thruster testing," *37th International Electric Propulsion Conference*, Boston, MA, USA, 2022. IEPC-2022-377.

[6] Walker, J. A., "Electrical facility effects on hall current thrusters: Electron termination pathway manipulation," *Journal of Propulsion and Power*, 2016.

[7] Dankanich, J. W., "Recommended practice for pressure measurement and calculation of effective pumping speed in electric propulsion testing," *Journal of Propulsion and Power*, 2017.

[8] Choueiri, E. Y., "Plasma oscillations in hall thrusters," *Physics of Plasmas*, 2001.

[9] Fife, J., Martinez-Sanchez, M., Szabo, J., Fife, J., Martinez-Sanchez, M., and Szabo, J., "A numerical study of low-frequency discharge oscillations in Hall thrusters," *33rd Joint Propulsion Conference and Exhibit*, 1997, p. 3052.

[10] Barral, S., and Ahedo, E., "Theoretical study of the breathing mode in Hall thrusters," *42nd AIAA/ASME/SAE/ASEE Joint Propulsion Conference & Exhibit*, 2006, p. 5172.

[11] Troyetsky, D. E., Greve, C. M., Tsikata, S., and Hara, K., "State estimation for real-time analysis of dynamic plasma properties and electrical circuit effects in Hall effect thrusters," *37th International Electric Propulsion Conference*, Cleveland, OH, USA, 2022. IEPC-2022-323.

[12] Piñero, L. R., "The Impact of Harness Impedance on Hall Thruster Discharge Oscillations," *NASA/TM-2017-219722*, 2017.

[13] Brieda, K. J., L., and Scharfe, M., "Influence of a Power Supply Model on Simulated Hall Thruster Discharge Voltage Oscillations," *AIP Advances*, Vol. 9, No. 2, 2019, pp. 1–5.

[14] Krishnan, A., "Impedance Analysis of the Hall Thruster Discharge Circuit and Plasma Load to Address Harness Facility Effects," *38th International Electric Propulsion Conference*, Toulouse, France, 2024. IEPC-2024-619.

[15] Barral, S., "Numerical investigation of closed-loop control for Hall accelerators," *Journal of Applied Physics*, 2011.

[16] Wei, L., "Stabilizing Low Frequency Oscillation with Two Stages Filter in Hall Thrusters," *34th International Electric Propulsion Conference*, Shanghai, China, 2015. IEPC-2015-284.

[17] Wei, L., "On the frequency characteristic of inductor in the filter of Hall thrusters," *Journal of Vacuum Science and Technology*, 2010.

[18] Wei, L., "Experimental study on the role of a resistor in the filter of Hall thrusters," *Physics of Plasmas*, 2011.

[19] Kieckhafer, A. W., "Recirculating liquid nitrogen system for operation of cryogenic pumps," *32nd International Electric Propulsion Conference*, Kurhaus, Wiesbaden, Germany, 2011. IEPC-2011-217.

[20] Greve, C. M., Majji, M., and Hara, K., "Real-time state estimation of low-frequency plasma oscillations in Hall effect thrusters," *Physics of Plasmas*, Vol. 28, No. 9, 2021, p. 093509. https://doi.org/10.1063/5.0057751.

[21] Troyetsky, D., Greve, C., Tsikata, S., and Hara, K., "State estimation of the dynamic behavior of plasma properties in a Hall effect thruster discharge," *Journal of Physics D: Applied Physics*, Vol. 56, No. 44, 2023, p. 444001.

[22] Hara, K., Sekerak, M. J., Boyd, I. D., and Gallimore, A. D., "Perturbation analysis of ionization oscillations in Hall effect thrusters," *Physics of Plasmas*, Vol. 21, No. 12, 2014, p. 122103. https://doi.org/10.1063/1.4903843.

[23] Biagi, S. F., "Biagi database v8.97," , 2015. URL www.lxcat.net.

[24] Hobbs, G., and Wesson, J., "Heat flow through a Langmuir sheath in the presence of electron emission," *Plasma Physics*, Vol. 9, No. 1, 1967, p. 85.

[25] Barral, S., Makowski, K., Peradzyński, Z., Gascon, N., and Dudeck, M., "Wall material effects in stationary plasma thrusters. II. Near-wall and in-wall conductivity," *Physics of Plasmas*, Vol. 10, No. 10, 2003, pp. 4137–4152.